Available online at www.sciencedirect.com
ScienceDirect
International Journal of Heat and Fluid Flow 28 (2007) 1178–1189
International Journal of HEAT AND FLUID FLOW
www.elsevier.com/locate/ijhff

The effects of axis ratio on laminar fluid flow around an elliptical cylinder

Zakir Faruquee [a], David S-K. Ting [a,*], Amir Fartaj [a], Ronald M. Barron [b], Rupp Carriveau [c]

[a] Department of Mechanical, Automotive and Materials Engineering, University of Windsor, Windsor, Ont., Canada N9B 3P4
[b] Department of Mathematics and Statistics, University of Windsor, Windsor, Ont., Canada N9B 3P4
[c] Department of Civil and Environmental Engineering, University of Windsor, Windsor, Ont., Canada N9B 3P4

Received 3 May 2006; received in revised form 15 October 2006; accepted 17 November 2006
Available online 2 February 2007

Abstract

An elliptical cylinder is a generic shape which represents a flat plate at its minor to major axis ratio (AR) limits of zero and infinity, and a circular cylinder at AR of unity. While incompressible flows over a streamwise flat plate (AR = 0), a cross-stream flat plate (AR = ∞), and a circular cylinder have been studied extensively, the role of AR on the detailed flow structure is still not well understood. Therefore, a numerical study was conducted to examine the flow field around an elliptical cylinder over a range of ARs from 0.3 to 1, with the major axis parallel to the free-stream, at a Reynolds number of 40 based on the hydraulic diameter. The control volume approach of FLUENT was used to solve the fluid flow equations, assuming the flow over the cylinder is unbounded, steady, incompressible and two-dimensional. It has been found that a pair of steady vortices forms when AR reaches a critical value of 0.34; below this value no vortices are formed behind the elliptical cylinder. Various wake parameters, drag coefficient, pressure and velocity distributions, have been characterized as functions of AR. The wake size and the drag coefficient are found to increase with the increase of AR. Quadratic correlations have been obtained to describe the relations of wake length and drag coefficient with axis ratio.

Keywords: Elliptical cylinder; Axis ratio; Confluence point; Cross-flow; Wake length

1. Introduction

Cylinders of different cross-sectional shapes (e.g., circular, elliptical, rectangular) are the basic building blocks of many engineering applications such as heat exchangers, nuclear reactors, and offshore structures. In practice, cylinders may be subjected to unbounded flow, where the effect of neighboring structures is negligible (such as flow around isolated offshore structures, towing cables, electric poles), or to bounded flow where the influence of neighbouring structures is significant. The fluid flow around an isolated cylinder placed in an open atmosphere is considered as unbounded flow. Therefore, due to its engineering significance, the flow around an isolated cylinder has motivated a large number of researchers to investigate the flow physics and engineering applications through theoretical, experimental and, more recently, computational approaches. Among them, circular cylinders have received widespread applications. In particular, the flow over a circular cylinder has been thoroughly investigated (Zdravkovich, 1997). The following subsection reviews the literature on the fluid flow over an unbounded circular cylinder.

1.1. Flow over a circular cylinder

As a uniform velocity flow approaches the leading point of a circular cylinder, the fluid is brought to rest, causing a pressure rise and the development of a boundary layer

* Corresponding author. Tel.: +1 519 253 3000x2599; fax: +1 519 973 7007.
E-mail address: dting@uwindsor.ca (D.S-K. Ting).

0142-727X/$ - see front matter © 2006 Elsevier Inc. All rights reserved.
doi:10.1016/j.ijheatfluidflow.2006.11.004

Nomenclature

a	semi-major axis [m]
AR	axis ratio, AR $= b/a$
b	semi-minor axis [m]
b_w	width of the wake at the maximum outer boundary [m]
C_f	skin friction coefficient, $C_f = \tau/(0.5\rho u_\infty^2)$
C_D	drag coefficient, $C_D = F_D/(0.5\rho u_\infty^2 L)$
C_p	pressure coefficient, $C_p = (p_s - p_\infty)/(0.5\rho u_\infty^2)$
d	hydraulic diameter of the cylinder [m]
F_D	drag force [N]
L	characteristic length [m]
L_w	wake length [m]
p	pressure [Pa]
q	speed [m/s]
r	radial distance [m]
Re	Reynolds number, $Re = (\rho u_\infty d)/\mu$
S	cross-stream distance between vortex centers [m]
u	x-component of the velocity [m/s]
v	y-component of the velocity [m/s]
x	streamwise direction
x_c	streamwise distance of vortex centers from the center of the cylinder [m]
y	cross-stream direction
y_c	cross-stream distance of vortex centers from the streamwise rear axis

Greek symbols

τ	shear stress [N/m^2]
μ	dynamic viscosity of air [N s/m^2]
ρ	density of air [kg/m^3]
θ	angular position along the cylinder surface [°]
Φ	velocity or pressure at any iteration

Subscripts

c1	first critical value
c2	second critical value
crl	critical value based on wake length
crd	critical value based on drag coefficient
f	viscous
p	pressure
fa	streamwise front axis
ra	streamwise rear axis
s	value on surface
va	vertical axis
w	wake
∞	free-stream

along the cylinder surface. The leading point of the cylinder is called the forward stagnation point. As long as the Reynolds number (Re) is less than 5, the flow splits into two symmetrically equal parts and passes around the cylinder to the rear stagnation point.

The pressure is relatively high at the forward stagnation point, because the kinetic energy associated with the flow is converted to pressure as the flow decelerates to zero at this leading point. The flow accelerates around the front portion of the cylinder where the pressure gradient is favorable (i.e., $\partial u/\partial x > 0$ when $\partial p/\partial x < 0$, where x is the streamwise distance along the cylinder from the forward stagnation point, u is the local streamwise velocity in the x direction, and p is the pressure). The flow reaches a maximum velocity when $\partial p/\partial x = 0$, beyond which it decelerates due to the adverse pressure gradient ($\partial u/\partial x < 0$ when $\partial p/\partial x > 0$). For $Re < Re_{c1}$ (where subscript "c1" signifies the 1st critical Re), the fluid flows around the cylinder all the way to the rear stagnation point of the cylinder. An increase of Re beyond Re_{c1} raises the adverse pressure gradient on the rear part of the cylinder, causing the fluid to decelerate on the rear half of the cylinder. The velocity gradient normal to the cylinder surface, $\partial u/\partial y|_{y=\text{surface}}$, (where y is the cross-stream direction, perpendicular to the cylinder surface), eventually becomes zero, at which point the fluid near the surface lacks sufficient momentum to overcome the pressure gradient, causing it to separate from the cylinder surface and form a steady recirculation bubble at the rear end of the cylinder.

Experimental estimates of the onset of the first critical Reynolds number have been reported in the literature. Taneda (1956) and Coutanceau and Bouard (1977) have reported the values of Re_{c1} as 5 and 4.4, respectively. Marris (1964) suggested $Re_{c1} = 5$, which was later reviewed and confirmed by Lienhard (1966). More recently, $Re_{c1} = 5$ was predicted from numerical stability analysis by Noack and Eckelmann (1994). The variation in these experimental findings is primarily due to the very small size of the eddies which develop in the immediate vicinity of the rear stagnation point of the cylinder, where the velocity is extremely small. Hence, it is difficult to detect the eddies immediately upon their emergence, either by visual images or velocity measurement. The recirculation zone remains steady, two-dimensional and symmetrical about the streamwise center line of the flow until a subsequent transition to periodic flow occurs at Re_{c2}, known as the 2nd critical Reynolds number. For $Re_{c1} < Re < Re_{c2}$, the length of the wake varies approximately linearly with the change of Re. The flow remains laminar, two-dimensional and steady, but can become unstable under the influence of external excitation.

This second transition or critical Reynolds number, Re_{c2}, was determined experimentally to have value of 40 by Kovasznay (1949) and Roshko (1954). When the Reynolds number is increased beyond 40, not every destabiliza-

tion of the flow, random or not, can be damped out (Braza et al., 1986). This leads to an asymmetrical eddy pattern, generating the alternating separation of vortices, which are shed, convected and diffused downstream of the cylinder, forming the well-known von Karman vortex street. Conceptually, the origin of the symmetric pattern destruction can be explained by the presence of multiple perturbation sources, such as non-uniform inlet conditions, irregularity of the boundary conditions, or disturbances in the flow conditions in the physical scenario (Braza et al., 1986). Nishioka and Sato (1978), while conducting experiments with a stationary cylinder in a low-speed wind tunnel, observed the first occurrence of weak sinusoidal fluctuations of velocity near the wake stagnation point on the downstream edge of a pair of standing eddies behind the cylinder at Re of 48. Noack and Eckelmann (1994) predicted this transition to occur at Re of 54; however, the Galerkin method they used may have had too few modes to capture the instability accurately. Williamson (1988) conducted a series of careful experiments in a towing tank and found this second transition to occur at $Re_{c2} \approx 49$, which is now regarded widely as the more accurate value. Sheard et al. (2001, 2003) validated this finding using a spectral-element method, predicting $Re_{c2} \approx 47$. This is in excellent agreement with Dusek et al.'s (1994) numerically simulated value of $Re_{c2} \approx 47.1$, via the application of the theoretical Landau model. Therefore, the range of Re for the formation of a pair of standing symmetric vortices behind the circular cylinder can be set as $5 \lesssim Re \lesssim 47$.

From the above discussions, it is evident that there should be a pair of stable vortices behind a circular cylinder at $Re = 40$. These vortices can be characterized by the location of the outer boundary, position of vortex centers, and length and width of the wake formed by the two vortices. Taneda (1956) experimentally studied the variation of the wake length as a function of Re. Coutanceau and Bouard (1977) experimentally determined all the parameters of the wake, i.e., length, cores' positions and wake outer boundary. Several authors have numerically determined the length of the wake, notable among them are Kawaguti (1953) and Silva et al. (2003).

The drag coefficient and the boundary layer separation angle for a circular cylinder were studied experimentally for low to moderate Re by several investigators (Tritton, 1959; Grove et al., 1964). The drag coefficient decreases and the angular position of boundary layer separation moves toward the front as Re is increased in the range of $5 \leqslant Re \leqslant 47$. Dennis and Chang (1970) and Silva et al. (2003) conducted numerical simulations to determine the drag coefficient and the boundary layer separation from the circular cylinder surface at $Re = 40$. These results are used to verify the current study.

1.2. Flow over an elliptical cylinder

While flow over a circular cylinder is well documented, literature on the broader family of elliptical cylinders (deformed circular cylinders) is very limited. Elliptical cylinders of various axis ratios (AR) ie., ratio of minor axis ($2b$) to major axis ($2a$), find application in heat exchangers, airfoils, and blades, among many others. The recent surge of interest in the use of elliptical cylinders in heat exchangers is partly due to their relatively smaller resistance to the flow compared to a circular cylinder (Khan et al., 2005; Li et al., 2005). This implies that the pumping requirement of a heat exchanger with elliptic tubes can be considerably smaller than that with circular tubes. Moreover, the smaller frontal area of elliptic tubes facilitates more compact heat exchanger design and is also beneficial in terms of particulate fouling of the outer surface in applications where severe fouling conditions prevail (Bouris et al., 2001; Khan et al., 2004).

Johnson et al. (2001, 2004) examined the effects of AR on the drag coefficient for AR in the range from 1 (circular cylinder) to ∞ (flat plate normal to the direction of flow) over the range of Re (based on the major axis perpendicular to the flow direction) from 30 to 200. They showed that the drag coefficient increases and the critical Reynolds number for the onset of vortex shedding decreases as AR increases. Several authors have investigated the flow past elliptical cylinders from moderate to high Reynolds numbers, notable among them are Lugt and Haussling (1974), Modi and Dikshit (1975), Ota et al. (1987), Modi et al. (1992) and Nair and Sengupta (1996).

It can be deduced from the analysis of the existing literature that data on the fluid flow over elliptical cylinders is limited, especially at low Reynolds numbers. Hence, the focus of this numerical study is to investigate the fluid flow around an elliptical cylinder at $Re = 40$ (based on hydraulic diameter). Specifically, the effects of axis ratio are explored by examining the shape of the wake, the pressure and the velocity distributions. To achieve this objective, two-dimensional, steady, incompressible uniform flow over elliptical cylinders with AR of 0.3, 0.4, 0.5, 0.6, 0.75 and 1 (circular cylinder) were simulated using FLUENT. Coutanceau and Bouard (1977) observed that measurements become very inaccurate at low Reynolds numbers, regardless of the experimental methods being used. Therefore, numerical simulation is a good complement for studying fluid flow around a cylinder when the Reynolds number is very small. The perimeters of all cylinders were kept constant throughout this study, in order to have the same reference (incoming) velocity.

2. Numerical models

2.1. Governing equations

Consider the physical model of a single cylinder subjected to a uniform upstream air flow in an open atmosphere. Flow over the cylinder is governed by the partial differential equations derived from the laws of conservation of mass (continuity equation) and momentum (Navier–Stokes equations). For incompressible steady flow, the con-

tinuity and momentum equations, together with appropriate boundary conditions, are solved for velocity and pressure distributions in the domain of interest. The two-dimensional continuity equation is given by

$$\frac{\partial u}{\partial x}+\frac{\partial v}{\partial y}=0, \tag{1}$$

where u and v are the x and y components of velocity, respectively. The x-direction momentum equation can be written as

$$u\frac{\partial u}{\partial x}+v\frac{\partial u}{\partial y}=-\frac{1}{\rho}\frac{\partial p}{\partial x}+\frac{\mu}{\rho}\left(\frac{\partial^2 u}{\partial x^2}+\frac{\partial^2 u}{\partial y^2}\right), \tag{2}$$

and the y-direction momentum equation can be expressed as

$$u\frac{\partial v}{\partial x}+v\frac{\partial v}{\partial y}=-\frac{1}{\rho}\frac{\partial p}{\partial y}+\frac{\mu}{\rho}\left(\frac{\partial^2 v}{\partial x^2}+\frac{\partial^2 v}{\partial y^2}\right), \tag{3}$$

where ρ is the density, p is pressure and μ is the dynamic viscosity. The assumption that the flow is two-dimensional implies that the cylinder is considered to be infinitely long, so that the end effects are negligible. Furthermore, we have assumed that the air is incompressible and the flow is laminar, since only low Reynolds number flow is being considered.

The governing equations (1)–(3) have been applied in the computational domain (Fig. 1) of the physical model. The annular computational domain implemented in this study is similar to one adopted by Mittal and Balachandar (1996). To minimize the effect of the far-field boundary conditions, the circular outer boundary of the computational domain must be placed sufficiently far away from the cylinder. A computational domain extending up to a radius of $10d$ (i.e., 10 diameters or 20 radii) from the center of the computational domain was initially employed. Then, to determine an appropriate location for the outer boundary, the computational domain was extended to $15d$, $20d$, $30d$, $40d$, $50d$ and $60d$. In all cases, the same cell distribution was used for common subdomains. The influence of the far-field boundary on the drag coefficient and wake length for a circular cylinder is given in Table 1 at $Re=40$. As seen from this table, moving the outer boundary from a radial distance of $30d$–$40d$ from the center of the cylinder does not have any noticeable effect on the flow parameters. Therefore, an annular computational domain having an outer radius of $40d$ was chosen to simulate the unbounded flow past the cylinders. Behr et al. (1995) studied the influence of the location of the lateral boundaries on the unsteady flow past a circular cylinder at $Re=100$. They have suggested that the lateral boundaries should be away from the cylinder by a distance of at least 8 cylinder diameters. In our case, which is a steady flow, the upstream, downstream and lateral distances of the far-field are much greater than those used by Behr et al. (1995).

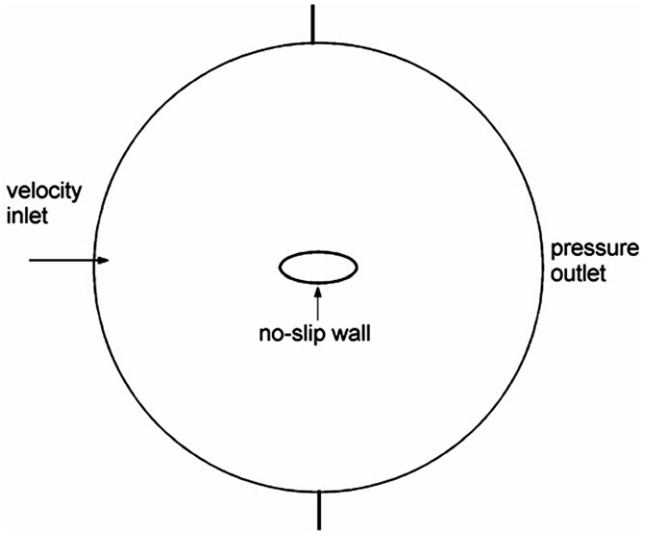

Fig. 1. Schematic of computational domain and boundary conditions.

Table 1
Effect of far-field boundary on the drag coefficient and wake length for a circular cylinder at $Re=40$

Far-field boundary radius	No. of cells	C_D	L_w/d
$10d$	32,400	1.63	2.28
$15d$	48,600	1.57	2.28
$20d$	64,800	1.55	2.28
$30d$	97,200	1.53	2.27
$40d$	129,600	1.52	2.27
$50d$	162,000	1.52	2.27
$60d$	194,400	1.51	2.27

The application of appropriate boundary conditions at the cylinder surface and at the outer boundary is crucial for accurate simulation. A uniform approach velocity was imposed on the upstream half circumference of the outer boundary of the computational domain, while a pressure outlet condition was imposed on the downstream half of the outer circumference of the computational domain (see Fig. 1). The pressure outlet condition was chosen for two reasons: the pressure at the exit is known (atmospheric) and it does not require the exit flow to be fully developed. No-slip condition was applied along the elliptical cylinder.

The control volume approach, using the Computational Fluid Dynamics (CFD) code FLUENT, with the implicit formulation and segregated solver was utilized for the solution of Eqs. (1)–(3). FLUENT uses an upwind/central differencing scheme, in which the convection terms are discretized using upwinding, and the diffusion terms are centrally differenced. FLUENT also offers the QUICK scheme to approximate the convective terms, which is based on averaging the second order upwind and central differences of a variable. In this study, the QUICK method of interpolation was used for solving velocity and momentum. The SIMPLEC method was employed for the pressure–velocity coupling for all simulations. This method is very good for laminar flow, where the convergence is limited by the pressure–velocity coupling (FLUENT Users' Manual, 2002). The second order interpolation scheme

was applied for pressure. The details of these methods can be found in Patankar (1980) and FLUENT Users' Manual (2002). The solution algorithm for the non-linear algebraic equations involves the linearization of the discretized equations and solution of the resultant linear equation system to yield updated values of the dependent variables, starting with given initial values and boundary conditions. In this work, the update continues until the relative difference between two successive iterations satisfies the following criterion:

$$\frac{|\phi^{k+1} - \phi^k|}{\phi^k} \leqslant 10^{-6}, \tag{4}$$

where ϕ^k represents pressure and velocities at the kth iteration. The tolerances for the relative differences between two successive iterations were also selected as 10^{-2}, 10^{-4}, 10^{-6}, 10^{-8} and their effect on the drag coefficient was studied. The value of 10^{-6} was found to be sufficient and was applied for all subsequent simulations reported here.

2.2. Mesh independence

Generally, the accuracy of a numerical solution increases as the number of cells increases. However, the use of a larger number of cells is restricted by the sophistication of the computer hardware and the computing time. The error that arises due to the discretization process can be systematically reduced to zero, at least theoretically, by subsequent grid refinements. All simulations performed in this study employed an O-type body-fitted grid system with quadrilateral cells. Grid spacing was gradually increased from the cylinder surface towards the outer boundary in order to avoid sudden distortion and skewness, and provide a sufficiently clustered mesh near the solid cylinder where the flow gradients are large. However, it was found that a large number of cells were required to obtain grid independent results, especially for the rear axis velocity in the wake region. The required total number of cells in the computational domain was reduced by increasing the number of cells near the cylinder and in the wake region by using a successive stretching ratio of 1.001 in both the radial and tangential directions.

Grid independency was achieved in this study according to the procedure outlined by Freitas (1999). Several meshes, with increasing refinement, were tested to ensure that the solution was independent of the mesh. These meshes, and the drag coefficient (C_D) and wake length (L_w) predictions are reported in Table 2 for the case of a circular cylinder at $Re = 40$. As can be seen from this table, a grid system with 360 nodes in the circumferential direction and 460 nodes in the radial direction under-predicts both the wake length and drag coefficient, whereas the results do not vary for meshes finer than 480×600. Thus, all results reported here are for simulations using 288,000 (480×600) cells in a computational domain with outer boundary having a radius of $40d$.

Table 2
Effects of cell density on flow parameters for a circular cylinder at $Re = 40$

Grid size ($\theta \times r$)	Minimum radial cell length near cylinder [d]	Wake length [L/d]	Drag coefficient [CD]
120×60	65.83×10^{-2}	1.34	1.177
180×360	10.97×10^{-2}	2.25	1.507
360×360	10.97×10^{-2}	2.25	1.490
360×460	85.58×10^{-3}	2.26	1.506
480×600	65.83×10^{-3}	2.31	1.526
960×1500	26.33×10^{-3}	2.31	1.525

3. Results and discussion

Simulations were conducted to study the effects of axis ratio (AR) on the fluid flow around a cylinder at $Re = 40$, over the range of ARs from 0.3 to 1. In particular, the correlations between AR and wake characteristics, velocity profiles and drag have been established.

3.1. Wake

The wake region is defined as the region behind the cylinder where eddies are formed and the local fluid velocity is less than the free-stream velocity (Zdravkovich, 1997). It is well-established that a steady state wake, or standing wake, forms behind a circular cylinder for Re in the range $5 \lesssim Re \lesssim 47$. A steady state wake is usually characterized by its length L_w, positions of the core (centers of the eddies) x_c and (cross-stream distance between vortex centers) S, and the outer boundary of the wake b_w, shown schematically in Fig. 2. The length of the wake, L_w, is typically defined as the streamwise distance between the confluence point (wake stagnation point) and the rear stagnation point of the cylinder. The confluence point is the point on the streamwise rear axis where the magnitude of the velocity is zero. The flow from the confluence point along the rear axis to the rear stagnation point of the cylinder moves upstream, whereas the flow from the wake stagnation point to the exit of the computational domain is towards the downstream. The velocities just cross-stream of the confluence point are directed toward each other, into the confluence point.

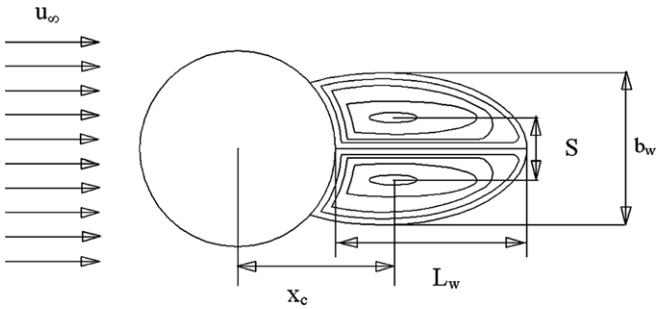

Fig. 2. Schematic of wake characteristics.

3.1.1. Wake length

In agreement with the existing experimental data (Williamson, 1988), the simulation predicts a pair of stable and symmetrical vortices behind a circular cylinder at $Re = 40$. The closed wake of a circular cylinder consisting of a pair of counter-rotating eddies ceases to exist if the Reynolds number is decreased below a critical Reynolds number ($Re_{cl} \approx 5$). Reducing AR has a similar effect as decreasing Re, that is, the size of the closed wake decreases with decreasing AR, and there exists a critical AR below which we would expect this wake to disappear. The pathlines for the flow over a circular cylinder show a pair of standing eddies (stable and symmetrical vortices) with a straight tail, consistent with the experimental findings of Taneda (1956). It is found, in this study, that elliptical cylinders with AR = 0.4, 0.5, 0.6, 0.75 also generate similar counter-rotating vortices with a straight tail. However, no eddies are found behind the elliptical cylinder with AR = 0.3. This indicates that the critical AR for the formation of a wake at $Re = 40$ is in the range $0.3 < AR_{crl} < 0.4$. The decreasing wake size and the disappearance of the standing eddies are expected, since the cylinder becomes progressively more streamlined and the obstruction to the flow is decreased with decreasing AR.

The length of the wake has been determined from the plots of streamline and velocity vectors, and also from the plot of rear axis velocity along the streamwise central line. Nishioka and Sato (1974) and Coutanceau and Bouard (1977) have noted that the wake length determined from the plot of velocity along the streamwise rear axis behind the cylinder would give a more accurate estimation of the wake length. In our opinion, these authors are correct because the streamwise rear axis velocity, downstream of the rear stagnation point, only crosses the streamwise rear axis at a single point defined as the confluence or wake stagnation point, which is easy to determine. The non-dimensional wake length obtained for different cylinders are plotted against the axis ratio in Fig. 3. The following quadratic curve fits the data, in a least square sense:

$$\frac{L_w}{d} = 2.24AR^2 + 0.50AR - 0.43. \quad (5)$$

The lower critical value of AR is found to be 0.34 ($AR_{crl} = 0.34$) from the extrapolation of the AR – L_w curve (see Fig. 3). This means that AR = 0.34 defines the lower limit for the formation of a wake behind an elliptical cylinder for this Reynolds number, and a wake forms behind an elliptical cylinder having AR > 0.34 at $Re = 40$. The critical axis ratio was also determined for different Re and is listed in Table 3, AR_{crl} was found to decrease with increasing Re. Coutanceau and Bouard (1977) experimentally determined the wake length for flow over a circular cylinder for blockage ratios (cylinder to test section area ratio) of 0.024, 0.07, 0.12 and extrapolated the wake length for zero blockage ratio, i.e., unbounded flow at $Re = 40$. Their extrapolated wake length is $2.13d$, which forms the lower bound of all data points (see Fig. 3, AR = 1). Silva et al. (2003) numerically found the wake length to be $2.51d$ for the unbounded circular cylinder, which sets the upper bound. The wake length determined in the present study falls between these lower and upper bounds, confirming the accuracy of the current simulation.

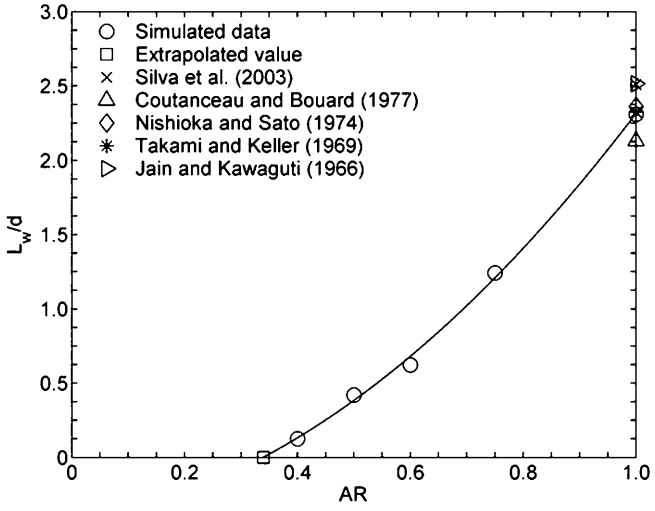

Fig. 3. Effect of AR on wake length. See the above mentioned reference in figure for more detail.

3.1.2. Wake core

Wake cores (vortex centers) are defined in terms of their x coordinate as $(x_c - a)/d$, i.e., non-dimensional distance from the rear stagnation point of the cylinder, and y coordinate as $y_c/d = 0.5S/d$ from the rear axis (see Fig. 2). The vortex centers can clearly be seen in the photographs taken by Taneda (1956) but their locations have not been quantified. Grove et al. (1964) and Coutanceau and Bouard (1977) measured the distances of the vortex centers from the circular cylinder rear stagnation point and from the near wake axis (streamwise rear axis) and scaled to the diameter of the cylinder. The vortex centers are determined in this study from the plots of velocity vectors and pathlines. After determining the vortex centers from the plot of velocity vectors, velocity was plotted across the cross-stream direction on a line joining the vortex centers of the wake. The magnitude of velocity is found to be zero at the vortex centers, verifying that the vortex centers obtained from the plots of velocity vectors or pathlines are accurate.

The magnitude of velocity plot across the line joining the wake centers of the circular cylinder is W-shaped, consistent with the experimental finding of Nishioka and Sato

Table 3
Effect of Re on critical ARs

Re	AR_{crl}	AR_{crd}
5	1	0.91
10	0.75	0.82
20	0.5	0.72
30	0.43	0.65
40	0.34	0.6

(1974). Similarly, W-shaped magnitude of velocity profiles exist in the wakes of elliptical cylinders with AR ranging from 0.4 to 0.75. The velocity above the upper wake's core and below the lower wake's core is in the direction of the free-stream velocity. The velocity at the vortex centers is zero and the velocity between the two vortex centers are toward the cylinder (opposite to the direction of main stream flow), which reaches its maximum value on the line joining the rear stagnation point of the cylinder and wake stagnation or confluence point. The centers of the vortices formed behind the circular cylinder were found at a streamwise distance of $1.23d$ from the center of the cylinder ($0.73d$ from the rear stagnation point of the cylinder) and at a cross-stream distance of $\pm 0.29d$ from the wake axis. These are in good agreement with the findings of Coutanceau and Bouard (1977) for an unbounded cylinder, who estimated the distances as $0.76d$ (from the rear stagnation point) and $\pm 0.295d$, respectively. The streamwise length of the wake core centers from the rear stagnation point $(x_c - a)/d$ is plotted in Fig. 4a and the cross-stream distance between the vortex centers (S/d) is plotted in Fig. 4b, for different ARs. It is seen that the streamwise coordinate $(x_c - a)/d$ of the vortex centers varies linearly with AR, on the other hand, the lateral distance between the wake centers is found to be approximately quadratically related with AR.

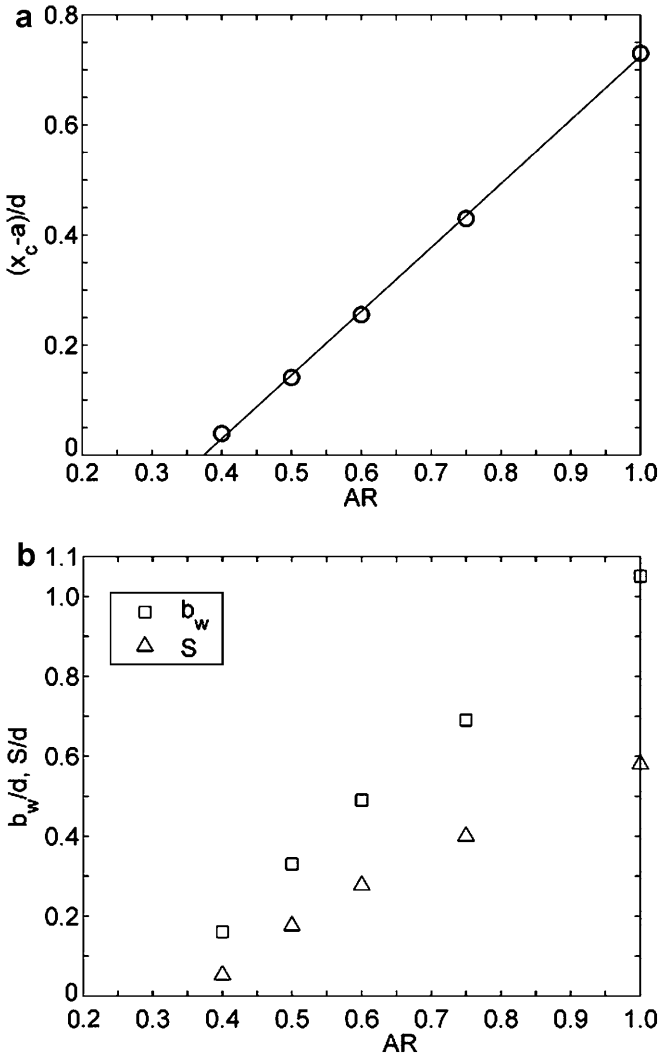

Fig. 4. Effect of AR on: (a) streamwise vortex centers position, (b) cross-stream distance of vortex centers and maximum wake width.

3.1.3. Wake outer boundary

The wake boundary is very important as it separates the vortex type flow within the wake from the outer flow past the cylinder and the wake. The wake's outer boundary has been obtained by following the velocity vectors from the upper and lower separation points toward the wake stagnation or confluence point. The wake's outer boundary can also be determined from the streamline emerging from the boundary layer separation points on the cylinder surface and extending to the wake stagnation point. The maximum width of the wake's outer boundary, b_w, for different ARs is plotted in Fig. 4b, scaled with respect to the diameter of the cylinder, and shows a linear variation. For Re_{c1} (critical Re corresponding to first separation of the boundary layer), the maximum width of the wake is at the separation point, and it moves gradually downstream from the separation point as Re is increased, but remains located upstream of the centers of the recirculating cores. The ratio of the distance between the cores (S) and the maximum width of the near-wake was found to be 0.56 for the circular cylinder, compared to 0.55–0.58 obtained by Zdravkovich (1997). The streamwise position of the maximum wake boundary for the circular cylinder is $1.08d$ from the center of the cylinder and $0.15d$ upstream of the wake's cores (centers), which is consistent with the literature (Zdravkovich, 1997). The streamwise position of maximum width of the wake in the case of elliptical cylinders with AR in the range of $0.4 \leqslant \mathrm{AR} \leqslant 0.75$ is also found upstream of the respective wake centers. No data for the closed wake of an elliptical cylinder was found in the literature to compare with the data obtained in this study. The plot of outer boundaries of the closed wake is given in Fig. 5 for different ARs.

3.2. Velocity distribution

The effect of axis ratio on the velocity along the streamwise front axis, across the cross-stream vertical axis and along the streamwise rear axis is discussed in this section.

3.2.1. Front axis velocity

The streamwise line from the inlet of the computational domain to the forward stagnation point of the cylinder is referred to as the front axis. The x-component of velocity along this line is referred to as the front axis velocity (u_{fa}). The front axis velocity varies due to the obstruction of flow by the cylinder and the boundary layer that builds up over the cylinder surface. The approach velocity starts decreasing as soon as the flow feels the presence of the cylinder and continues to decrease, eventually to zero at the

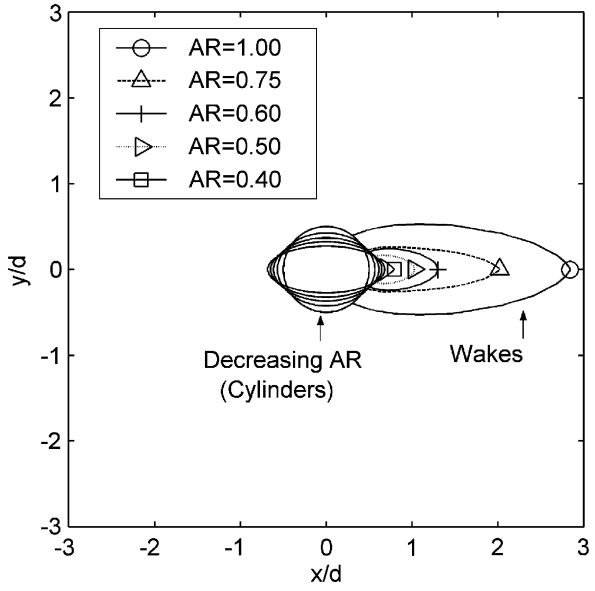

Fig. 5. Variation of wake outer boundary with AR.

forward stagnation point of the cylinder. The point where the oncoming fluid starts to retard depends on *Re* and AR for an unbounded flow. Although the onset of retardation begins at a far upstream position, the front axis velocity maintains 99% of the free-stream velocity up to approximately $8.75d$ upstream for $AR = 0.3$ and $10.5d$ for $AR = 1$, and between these limits for all the intermediate ARs considered. This region has attracted limited research despite the high heat transfer from the forward stagnation point (Zdravkovich, 1997). The non-dimensional front axis velocity (u_{fa}/u_∞) is given in Fig. 6a for different ARs from $10d$ upstream of the center of the cylinder to the forward stagnation point. The front axis velocities for different ARs first diverge and then converge to a neutral point, where the velocity profiles cross each other at $0.86d$ upstream of the center of the cylinder, and again diverge and become zero at the respective forward stagnation point of the cylinders. The front axis velocity upstream of the neutral point decreases as AR is increased, i.e., it is maximum for the elliptical cylinder with $AR = 0.3$ and is minimum for $AR = 1$. This is attributed to the fact that the cylinder with lower AR is more streamlined, as a consequence the local blockage (obstruction to the flow by the cylinder) is reduced, causing less fluid to retard along the front axis of the cylinder. The opposite trend (i.e., front axis velocity decreases faster with lower axis ratio) is found from the neutral point to the forward stagnation point of the cylinder. This is due to the extension of the forward stagnation point toward the upstream with the reduction of AR.

3.2.2. Cross-stream vertical axis velocity

The cross-stream line passing through the center of the cylinder is identified as the vertical axis. The velocity across this vertical line is referred to as the vertical axis velocity,

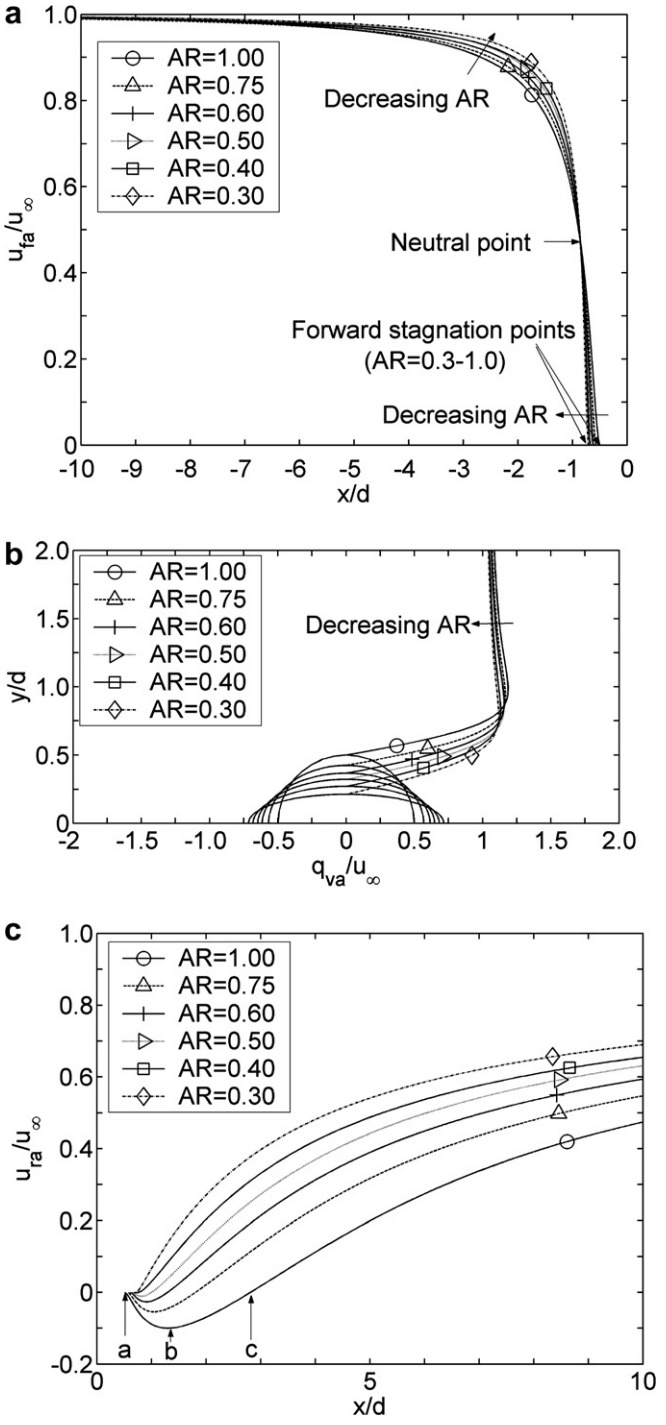

Fig. 6. Effect of AR on (a) front axis velocity, (b) cross-stream vertical axis velocity, (c) rear axis velocity (points a, b, c represent velocities of rear stagnation point, maximum returning and confluence point for the circular cylinder).

and is symmetrical with respect to the horizontal axis. The vertical axis velocity above the cylinder is portrayed in Fig. 6b up to a cross-stream distance of $2d$ from the center of the cylinder for AR in the range 0.3–1. The difference between the velocities occurs due to the variation of AR; the vertical axis velocity attains a maximum value for the circular cylinder and a minimum value for the elliptical cyl-

inder with AR = 0.3. The difference gradually diminishes as the cross-stream distance increases from the center of the cylinders. The magnitude of the maximum vertical axis velocity decreases gradually with the decrease of AR, and the distance between the position of maximum vertical axis velocity and the cylinder surface increases with the decrease of AR.

3.2.3. Rear axis velocity

The downstream line passing through the rear stagnation point of the cylinder and the wake stagnation point is referred to as the rear axis in the current study. Many authors have defined this line as the central line because it is situated between the two steady vortices. The velocity along this line is termed as the rear axis velocity. The velocity along the rear axis is plotted in Fig. 6c for different ARs. The rear axis velocity crosses zero at the wake stagnation point. The rear axis velocity is negative between the wake stagnation point and the rear stagnation point of the cylinder, indicating that the fluid returns toward the cylinder from the confluence point, reaches a maximum value, then decreases in magnitude and becomes zero at the rear stagnation point of the cylinder. Here the flow separates into two parts, one part follows the cylinder contour upward, the other part downward. For a circular cylinder, the magnitude of the maximum returning velocity was found to be about 10% of the free-stream velocity and its location was found at a distance of 1.3*d* from the center of the circular cylinder, which is in good agreement with the findings of Coutanceau and Bouard (1977). The line segment joining the wake stagnation point and rear stagnation point of the cylinder is known as the line of returning stagnation, which separates the upper vortex from the lower vortex. No fluid crosses the line of returning stagnation. The velocity at the downstream side of the confluence point in the direction of the free-stream velocity and its magnitude increases as it traverses downstream for some distance.

All cylinders that generate a wake have somewhat similar rear axis velocity profile. However, variation of the velocity depends strongly on AR, as portrayed in Fig. 6c. Initially, the magnitude of rear axis velocity at downstream of the confluence point increases with the decrease of AR in the direction of flow. Eventually, all rear axis velocities of cylinders with different ARs attain the free-stream velocity if the downstream computational domain is sufficiently large. On the other hand, the magnitude of returning (negative) velocity decreases with the decrease of AR in the range of $0.4 \leqslant \mathrm{AR} \leqslant 1$. The elliptical cylinder with AR = 0.3 does not have any returning velocity, confirming that no vortices form behind it. No data was found in the literature to compare the rear axis velocities of elliptical cylinders for different ARs.

3.3. Drag coefficient

The force on the cylinder is produced by the friction force along the surface of the cylinder and by the non-symmetric pressure distribution on the upstream and downstream side of the cylinder. Drag is the only force component that acts on the cylinder at $Re = 40$ because all flows at this Re are symmetrical with respect to the direction of flow (Lienhard, 1966). The drag force can be calculated from the pressure and shear stresses acting on the cylinder as

$$F_{\mathrm{D}} = \int p\cos\theta\,\mathrm{d}\theta + \int \tau\sin\theta\,\mathrm{d}\theta. \tag{6}$$

Alternatively, one can use the non-dimensional drag coefficient, defined as

$$C_{\mathrm{D}} = \frac{F_{\mathrm{D}}}{\frac{1}{2}\rho u_\infty^2 L} = C_{\mathrm{Dp}} + C_{\mathrm{Df}}, \tag{7}$$

where

$$C_{\mathrm{Dp}} = \frac{\int C_{\mathrm{p}}\cos\theta\,\mathrm{d}\theta}{L}; \quad C_{\mathrm{Df}} = \frac{\int C_{\mathrm{f}}\sin\theta\,\mathrm{d}\theta}{L}. \tag{8}$$

and

$$C_{\mathrm{p}} = \frac{p_{\mathrm{s}} - p_\infty}{\frac{1}{2}\rho u_\infty^2}; \quad C_{\mathrm{f}} = \frac{\tau}{\frac{1}{2}\rho u_\infty^2}. \tag{9}$$

In these equations, p_{s} is the pressure on the cylinder surface at angular position θ, p_∞ is the static pressure of free-stream air, τ is the shear stress and L is the appropriate characteristic length. Hence, the drag consists of skin friction drag due to viscous forces acting on the body, and pressure or form drag due to unbalanced pressure forces on the body. In the case of a circular cylinder $L = d$, and for an elliptical cylinder, $L = 2a$. The drag force can be determined from the above equations. The mean pressure coefficient (one of the components of C_{D}) of the cylinder is estimated from pressure distribution over the cylinder as explained in the next section.

3.3.1. Pressure coefficient distribution

The pressure along the cylinder surface is expressed by a non-dimensional quantity, C_{p}, known as pressure coefficient, defined by Eq. (9). At $Re = 40$, the distribution of C_{p} over the upper and lower halves of the cylinders is symmetrical. Pressure coefficients over the top half surface of the cylinder (0–180°) for different axis ratios are given in Fig. 7a. The value of C_{p} at the forward stagnation point of the cylinder is approximately 1 (this may differ depending on the reference pressure) for AR = 0.3–1. The pressure coefficient decreases along the circumference of the cylinder, reaches a minimum value (around an angular position of 90°) and then increases up to the rear stagnation point of the cylinder. Pressure coefficient C_{p} is strongly influenced by AR. The pressure drop becomes sharper at the frontal section with the decrease of AR. The minimum value of C_{p} indicates the change from a favorable to an adverse pressure gradient over the cylinder surface. The minimum value of C_{p} occurs at 89° for the circular cylinder and, for elliptical cylinders with $\mathrm{AR} < 1$, the minimum value of C_{p} takes place at an angular position greater than 90°

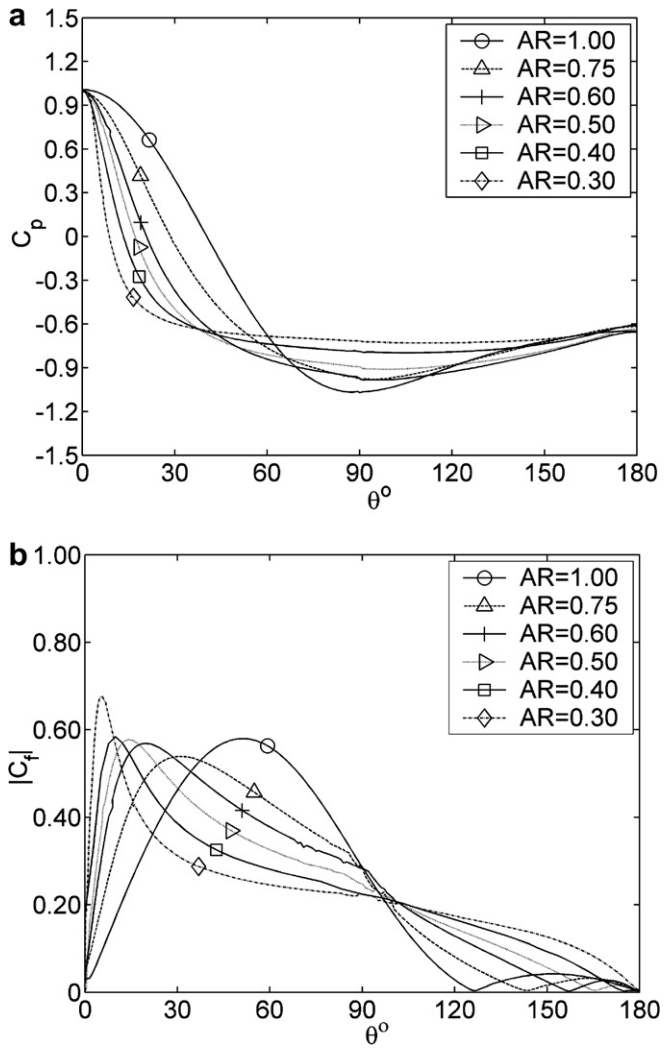

Fig. 7. (a) Pressure coefficient distribution for cylinders with different ARs, (b) skin friction coefficient for cylinders with different ARs.

with the angle increasing as AR decreasing. As the AR is decreased, the magnitude of minimum pressure coefficient decreases, and eventually becomes almost flat for AR = 0.3. In case of the elliptical cylinder with AR = 0.3, the higher favorable pressure gradient at the front of the cylinder and the lower adverse pressure gradient at the back of the cylinder aid the flow in inhibiting separation.

3.3.2. Skin friction coefficient distribution

The distributions of C_f over upper and lower halves of all cylinders are symmetrical about the streamwise centerline. Therefore, C_f distributions over the cylinders with different ARs are plotted in Fig. 7b for $\theta = 0$–$180°$, i.e., from the forward stagnation point to the rear stagnation point of the cylinder. The angular position of maximum C_f shifts toward the forward stagnation point with the decrease of AR. The second zero value of C_f indicates the boundary layer separation point from the cylinder surface, which moves toward the rear stagnation point of the cylinder with the decrease of AR. The magnitude of maximum C_f drops from the value of a circular cylinder as AR is lowered from 1 to 0.75. Then the maximum value of C_f gradually increases with decreasing AR and sharply increases for AR = 0.3. The value of maximum C_f for the cylinder with AR = 0.3 is found to be greater than the C_f of all other cylinders used in this study (see Fig. 7b). A similar trend was reported by Schlichting (1979) for AR of 1, 0.5, 0.25 and 0.125.

The mean pressure (form drag) coefficient of the cylinder is calculated by area weighted average of the local pressure coefficient over the cylinder surface. Similarly, the mean skin friction (viscous drag) coefficient is obtained by weighted area average of the local skin friction coefficient over the cylinder surface. The addition of these two gives the total drag coefficient (usually referred to as the drag coefficient) of the cylinder surface (see Eq. (7)). The C_D predicted in this study is 1.53 for the circular cylinder (AR = 1), compared to an experimental value of 1.48 (Tritton, 1959) and numerical value of 1.52 (Henderson, 1995). Grove et al. (1964) provided a correlation to estimate the pressure drag coefficient of a circular cylinder at low *Re* as

$$C_{Dp} = 0.62 + 12.6/Re. \tag{10}$$

This equation gives an estimate of $C_{Dp} = 0.935$, which is not significantly lower than the value of 1.00 obtained in this study, and results obtained by others; see Table 4. Dennis and Chang (1970) have given the following correlation for the friction drag coefficient of the circular cylinder:

$$C_{Df} = 1.83Re^{-0.5} + 9.95/Re. \tag{11}$$

This equation gives an estimate of $C_{Df} = 0.538$ against the value of $C_{Df} = 0.524$ obtained numerically by the same authors at $Re = 40$. The viscous drag coefficient obtained in this study for circular cylinder is $C_{Df} = 0.533$. A comparison of the existing drag coefficients in the literature is made with the data obtained in this simulation and is given in Table 4. No data was found to compare the drag coefficients for elliptical cylinders.

The total, viscous and pressure drag coefficients obtained in this study are given in Fig. 8 as functions of AR. The total drag and pressure drag coefficients of a circular cylinder are largest. Both the total drag and the pressure drag coefficients of the cylinders decrease with the

Table 4
Comparison of C_D for unbounded circular cylinder

Investigators	C_{Dp}	C_{Df}	C_D
Present study	1	0.53	1.53
Sahin and Owens (2004)	–	–	1.52
Silva et al. (2003)	–	–	1.54
Henderson (1995)	1.01	0.52	1.53
Dennis and Chang (1970)	0.998	0.524	1.522
Son and Hanratty (1969)	0.997	0.513	1.51
Tritton (1959)	–	–	1.48
Kawaguti (1953)	1.053	0.565	1.618

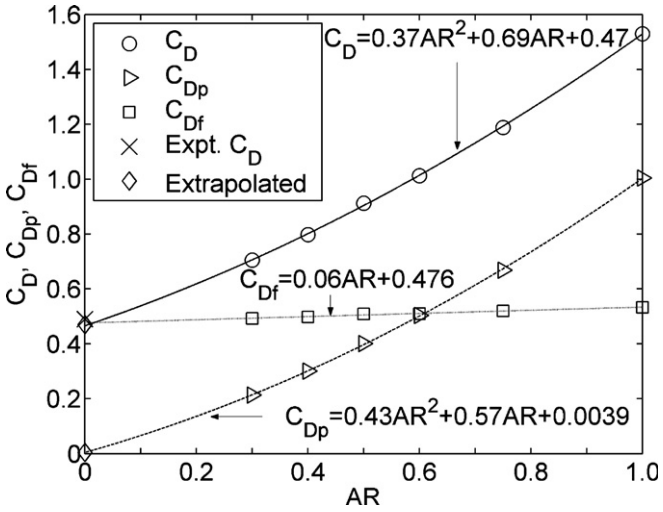

Fig. 8. Effect of AR on drag coefficient.

decrease of AR. The viscous drag coefficient also decreases, but very slowly, as AR is decreased. The viscous and pressure drag coefficients are equal at AR = 0.6. This value of AR is identified as the critical AR (AR_{crd}) based on drag coefficients. The pressure drag coefficient dominates for $AR > AR_{crd}$ and the viscous drag coefficient dominates for $AR < AR_{crd}$. Least square curves were used to fit the drag coefficient data. Extrapolation of these curves generate the drag coefficient for a streamwise flat plate of length 0.035 m (half the circumference of the cylinder). The following equations are obtained from the curve fitting to the data in Fig. 8:

$$C_D = 0.37AR^2 + 0.69AR + 0.465 \quad (12)$$

$$C_{Dp} = 0.43AR^2 + 0.57AR + 0.004 \quad (13)$$

$$C_{Df} = 0.0578AR + 0.476. \quad (14)$$

Inserting AR = 0 in Eqs. (12)–(14) gives $C_D = 0.465$, $C_{Dp} = 0.004$ and $C_{Df} = 0.476$ for a streamwise flat plate of length 0.035 m (1.57*d*). Theoretically, C_{Dp} should be zero for a streamwise thin flat plate and C_{Df} is the sole contributor to C_D. The current extrapolated C_D of 0.465 is in reasonable agreement with the experimental data in Schlichting (1979).

The critical axis ratio, AR_{crd} which leads to equal viscous and pressure drag, is also found for a range of low *Re* and is given in Table 3. The value of AR_{crd} is high at lower Reynolds number and decreases as *Re* is increased up to a value of 40.

4. Conclusions

This study was carried out to investigate the effects of axis ratio (AR) on the fluid flow around an elliptical cylinder at a Reynolds number of 40 based on hydraulic diameter. The conclusions drawn from the simulated results of unbounded fluid flow at $Re = 40$ over a rigid stationary cylinder with AR of 0.3–1 are given below:

(a) The unbounded flow around a cylinder is simulated by restricting the computational domain to a finite extent. A circular computational domain having a radius of 40*d* was found adequate for the current study.

(b) The simulated results of the wake shape, drag coefficient, and rear axis velocity agree very well with those available in the existing literature.

(c) The wake size increases as AR is increased from 0.4 to 1. No vortices were found behind the cylinder with AR = 0.3. An interpolated value of AR, defined as the critical AR_{crl} based on wake length was found to be approximately 0.34. When $AR > AR_{crl}$, a pair of steady vortices forms behind the cylinder and when $AR < AR_{crl}$, the steady pair of vortices disappears. AR_{crl} was found to decrease with increasing AR for $Re = 5$ to 40.

(d) The drag coefficient (C_D) is found to increase with the increase of AR. The drag coefficient is maximum for AR = 1 (circular cylinder). The viscous drag is found to increase very slowly, whereas the pressure drag increases rather sharply, with the increase of AR. The pressure (C_{Dp}) and viscous (C_{Df}) drag coefficients are almost equal for $AR_{crd} = 0.60$. The pressure drag coefficient is dominant for AR > 0.6 and the viscous drag coefficient is found to be dominant for AR < 0.6. The ratio of pressure to viscous drag coefficient (C_{Dp}/C_{Df}) is 1.89 for the circular cylinder and 0.43 for the elliptical cylinder with AR = 0.3. The ratio of pressure to total drag coefficient is 0.65 for the circular cylinder and 0.30 for the elliptical cylinder with AR = 0.3. The value of AR_{crd} is high at low Reynolds number and decreases as *Re* is increased up to a value of 40.

Acknowledgement

The authors are grateful to Natural Sciences and Engineering Research Council of Canada for providing financial support for this project.

References

Behr, M., Hastreiter, D., Mittal, S., Tezduyar, T.E., 1995. Incompressible flow past a circular cylinder: dependence of the computed flow field on the location of the lateral boundaries. Comput. Methods Appl. Mech. Eng. 123, 309–316.

Bouris, D., Papadakis, G., Bergeles, G., 2001. Numerical evaluation of alternate tube configurations for particle deposition rate reduction in heat exchanger tube bundles. Int. J. Heat Fluid Flow 22, 525–536.

Braza, M., Chassaing, P., Ha Minh, H., 1986. Numerical study and physical analysis of the pressure and velocity fields in the near wake of a circular cylinder. J. Fluid Mech. 165, 79–130.

Coutanceau, M., Bouard, R., 1977. Experimental determination of the main features of the viscous flow in the wake of a circular cylinder in uniform translation. Part 1. Steady flow. J. Fluid Mech. 79, 231–256.

Dennis, S.C.R., Chang, G., 1970. Numerical solutions for steady flow past a circular cylinder at Reynolds numbers up to 100. J. Fluid Mech. 42, 471–489.

Dusek, J., Le Gal, P., Fraunie, P., 1994. A numerical and theoretical study of the first Hopf bifurcation in a cylinder wake. J. Fluid Mech. 264, 59–80.

FLUENT Users' Manual, 2002. Computational Fluid Dynamics Software, Fluent Inc.

Freitas, C.J., 1999. The issue of numerical uncertainty. In: Proc. 2nd International Conference on CFD in the Minerals and Process Industries, CSIRO, Melbourne, Australia, pp. 29–34.

Grove, A.S., Shair, F.H., Petersen, E.E., Acrivos, A., 1964. An experimental investigation of steady separated flow past a circular cylinder. J. Fluid Mech. 19, 60–80.

Henderson, R.D., 1995. Details of drag curve near the onset of vortex shedding. Phys. Fluids 7, 2102–2104.

Jain, P.C., Kawaguti, M., 1966. Numerical study of a viscous fluid flow past a circular cylinder. J. Phys. Soc. Japan 21, 2055–2067.

Johnson, S.A., Thompson, M.C., Hourigan, K., 2001. Flow past elliptical cylinders at low Reynolds numbers. In: Proc. 14th Australian Fluid Mechanics Conference, University of Adelaide, Adelaide, Australia.

Johnson, S.A., Thompson, M.C., Hourigan, K., 2004. Predicted low frequency structures in the wake of elliptical cylinders. Eur. J. Mech. B/Fluids 23, 229–239.

Kawaguti, M., 1953. Numerical solution of the Navier–Stokes equations for the flow around a circular cylinder at Reynolds number 40. J. Phys. Soc. Japan 8, 747–757.

Khan, M.G., Fartaj, A., Ting, D.S.-K., 2004. An experimental characterization of cross-flow cooling of air via an in-line elliptical tube array. Int. J. Heat Fluid Flow 25, 636–648.

Khan, W.A., Culham, J.R., Yovanovich, M.M., 2005. Fluid flow around and heat transfer from elliptical cylinders: analytical approach. J. Thermophys. Heat Transfer 19, 178–185.

Kovasznay, L.S.G., 1949. Hot-wire investigation of the wake behind cylinders at low Reynolds number. Proc. Roy. Soc. A 198, 174–190.

Lienhard, J.H., 1966. Synopsis of lift, drag and vortex frequency data for rigid circular cylinders. College of Engineering, Research Division, Washington State University, Bulletin 300.

Li, Z., Davidson, J., Mantell, S., 2005. Numerical simulation of flow field and heat transfer of streamlined cylinders in crossflow. In: Proc. of HT2005, 2005 ASME Summer Heat Transfer Conference, July 17–22, San Francisco, California, USA, pp. 531–541.

Lugt, H.J., Haussling, H.J., 1974. Laminar flow past an abruptly accelerated elliptic cylinder at 45° incidence. J. Fluid Mech. 65, 711–734.

Marris, A.W., 1964. A review of vortex streets, periodic wakes, and induced vibration phenomena. J. Basic Eng. 86, 185–196.

Mittal, R., Balachandar, S., 1996. Direct numerical simulation of flow past elliptic cylinders. J. Comput. Phys. 124, 351–367.

Modi, V.J., Dikshit, A.K., 1975. Near-wakes of elliptic cylinders in subcritical flow. AIAA J. 13, 490–497.

Modi, V.J., Wiland, E., Dikshit, A.K., Yokomizo, T., 1992. On the fluid dynamics of elliptic cylinders. Int. J. Offshore Polar Eng. 2, 267–280.

Nair, M.T., Sengupta, T.K., 1996. Onset of asymmetry: flow past circular and elliptic cylinders. Int. J. Numer. Methods Fluids 23, 1327–1345.

Nishioka, M., Sato, H., 1974. Measurements of velocity distributions in the wake of a circular cylinder at low Reynolds numbers. J. Fluid Mech. 65, 97–112.

Nishioka, M., Sato, H., 1978. Mechanism of determination of the shedding frequency of vortices behind a cylinder at low Reynolds number. J. Fluid Mech. 89, 49–60.

Noack, B., Eckelmann, H., 1994. A global stability analysis of the steady and periodic cylinder wake. J. Fluid Mech. 270, 297–330.

Ota, T., Nishiyama, H., Taoka, Y., 1987. Flow around an elliptic cylinder in the critical Reynolds number regime. J. Fluids Eng. 109, 149–155.

Patankar, S.V., 1980. Numerical Heat Transfer and Fluid Flow. Taylor & Francis, USA.

Roshko, A., 1954. On the development of turbulent wakes from vortex streets. National Advisory Committee for Aeronautics, Report 1191.

Sahin, M., Owens, R.G., 2004. A numerical investigation of wall effects up to high blockage ratios on two dimensional flow past a confined circular cylinder. Phys. Fluids 16, 1305–1320.

Schlichting, H., 1979. Boundary-Layer Theory. McGraw-Hill Inc., New York, USA.

Sheard, G.J., Thompson, M.C., Hourigan, K., 2001. A numerical study of bluff ring wake instability. In: Proc. 14th Australian Fluid Mechanics Conference, University of Adelaide, Adelaide, Australia.

Sheard, G.J., Thompson, M.C., Hourigan, K., 2003. From spheres to circular cylinders: the stability and flow structures of bluff ring wake. J. Fluid Mech. 492, 147–180.

Silva, A.L.F.L.E., Silveira-Neto, A., Damasceno, J.J.R., 2003. Numerical simulation of two-dimensional flows over a circular cylinder using the immersed boundary method. J. Comput. Phys. 189, 351–370.

Son, J.S., Hanratty, T.J., 1969. Numerical solution for the flow around a cylinder at Reynolds numbers of 40, 200 and 500. J. Fluid Mech. 35, 369–386.

Takami, H., Keller, H.B., 1969. Steady two-dimensional viscous flow of an incompressible fluid past a circular cylinder. Phys. Fluids 12, 51–56.

Taneda, S., 1956. Experimental investigation of the wakes behind cylinders and plates at low Reynolds numbers. J. Phys. Soc. Japan 11, 302–307.

Tritton, D.J., 1959. Experiments on the flow past a circular cylinder at low Reynolds numbers. J. Fluid Mech. 6, 547–567.

Williamson, C.H.K., 1988. Defining a universal and continuous Strouhal–Reynolds number relationship for the laminar vortex shedding of a circular cylinder. Phys. Fluids 31, 2742–2744.

Zdravkovich, M.M., 1997Flow Around Circular Cylinders: Fundamentals, vol. 1. Oxford University Press Inc., New York, USA.